EuroSun2026

INVESTIGATING THE IMPACT OF GROUNDWATER ON THE THERMAL LOSSES OF UNDERGROUND LARGE THERMAL ENERGY STORAGE SYSTEMS

Summary

Underground thermal energy storage (TES) may face technical challenges in areas with shallow groundwater (GW), where advective heat transport increases thermal losses and raises GW temperature. Numerical modelling helps assess TES performance and quantify the impact on the ground, but accounting for GW flow increases the numerical effort and model complexity. In this work, a TES coupled with the surrounding ground is modelled in COMSOL Multiphysics. The effect of GW is investigated for both tank and shallow pit TES geometries. For the pit TES, three GW depths are analysed to assess their influence on TES losses and ground temperature. Results show that GW characteristics (depth relative to the TES stratification, and flow velocity) affect the distribution of thermal losses, the TES thermal stratification and the risk of GW overheating. This effect is most pronounced in absence of thermal insulation, when the total thermal losses can double for the investigated PTES cases and the downstream ground temperature shows an increase up to 20 K. Two approaches for modelling GW are compared: a coupled approach, solving GW flow and heat transfer at every time step, and a decoupled approach, in which the GW flow field is first solved as a stationary problem and the resulting velocity field is then applied in the energy balance of the saturated soil. The decoupled approach reduces the number of equations solved per time step, cutting simulation time by ≈22% over a 1 year operation period.

Thermal Energy Storage, Groundwater, modelling, thermal losses

Field of application for the findings: Thermal Energy Storage, Sustainable Energy Infrastructure

Addressed audience: scientific audience, planners, decision makers

1. Introduction

Supporting the energy transition in the building sector requires the integration of renewable energy (RE) sources, characterised by seasonal and daily oscillating availability. In district heating (DH) systems, thermal energy storage (TES) systems allow to decouple energy generation and demand to facilitate the integration of RE sources and are a key element of solar DH, but they can be effectively coupled also with cogeneration plants and power to heat technologies (IEA Energy Storage TCP 2024). A challenge of the integration of TES systems on the district scale is however related to the large volumes required, which call for underground systems in order to meet social acceptance in urban applications.

Water-based tank and pit TES allow high storage densities, discharge power and can reach storage temperatures up to 95 °C in underground configurations, hence representing a flexible integration solution within RE-based DH networks (Schmidt et al. 2018). A drawback of large scale TES systems is however related to the high investment costs (Lüchinger et al. 2025), although economies of scale make it possible to reduce the storage specific cost by increasing its size. Increasing the depth of underground water-based TES (whether tank or pit) increases the likelihood of reaching the groundwater (GW) table. With water storage temperatures up to 95°C, the thermal losses to the surrounding ground are significant and can elevate subsurface temperatures markedly. Field observations report subsurface temperatures approaching 30°C near seasonal TES installations in Hamburg and Friedrichshafen, Germany, evidencing warming of adjacent soil (Bott et al. 2024). Simulation studies corroborate the magnitude of the twofold interaction between TES and aquifers, showing that flowing GW increases TES heat losses relative to no-GW cases (Dahash et al. 2021). Moreover GW temperatures above 20°C can promote bacterial growth, which is particularly relevant for infrastructure siting near drinking water distribution networks. Temperature increase can increase contaminant mobility in aquifers and influence microbial abundance and community composition (Motamedi et al. 2026).

Despite the importance of GW, only few European countries have national regulations for the thermal use of subsurface (Haehnlein et al. 2010). For example, Austrian regulations require to endure a maximum GW temperature difference of ±6 K, a maximum GW temperature of 20°C and a minimum temperature of 5°C (ÖWAV 2009). Compared to the reference values provided by Haehnlein et al. (2010), the legal landscape changed less than expected. In the Netherlands, the large expansion of aquifer TES led to more detailed rules concerning maximum injection temperatures, thermal balance, monitoring, interference between systems (Blum et al. 2021). In order to minimize the interaction between TES and GW, geotechnical measures like cut-off walls, i.e. impermeable barriers used in geotechnics to restrict the horizontal movement of liquids, in combination with pumping wells can be considered (Dahash et al. 2021).

The effect of GW flow on TES performance using numerical models has been investigated by several authors. Dahash et al. (2021) conducted a detailed investigation on the twofold interaction between GW and TES using a finite element model of the TES coupled with the surrounding ground (and GW table) implemented in COMSOL Multiphysics. The authors also considered the role of thermal insulation and cut-off walls in reducing GW overheating. Sifnaios et al. (2023) investigated the possible effects of GW on the Marstal pit TES implementing a 3D model in ANSYS Fluent: in this study however the authors focused on the heat losses to the ground, while the water temperature inside the TES was applied as boundary condition. The authors also investigated different GW depths. Bott et al. (2024) applied a co-simulation approach to investigate the effect of GW flow on a buried water-gravel TES, modelled in MATLAB/Simulink, while a 3D multiphysical model of the surrounding ground and GW was implemented in COMSOL Multiphysics.

The lack of long-term field studies on the potential harming effects of increased GW temperatures reinforces the need for integrated hydrogeochemical monitoring and conservative thermal management to maintain groundwater quality and biodiversity near underground TES installations. Numerical modelling is a decision-support tool for anticipating and managing GW overheating around underground TES because it can resolve coupled GW flow and heat transport, predicting plume extent, peak temperatures, and storage thermal losses under site-specific hydrogeological conditions and operating strategies. These models capture advection, conduction, and thermal dispersion in porous media and can incorporate multiphysics couplings, allowing rapid testing of design variants (e.g., geometry, insulation) and operating regimes (e.g. seasonal vs. short term operation), as well as mitigation measures such as impermeable cut-off walls to reduce advective spreading—thereby supporting risk assessment and permitting while minimizing environmental impact.

Although GW-coupled TES modelling has been addressed in the literature, the associated computational effort — a key factor for the feasibility of large-scale, long-term simulations — has received little to no systematic attention. Within the framework of the IEA ES TCP Task 45, various TES models are being verified, and their ability to represent the effects of GW is compared.

This work compares the computational time required to simulate the dynamic behaviour of ground-coupled TES systems under the effect of GW. The two most common large-scale TES geometries —tank and pit— are considered, and the effect of GW on the thermal stratification of the storage is investigated. Particular focus is placed on the uninsulated pit TES, analysing the impact of GW depth and flow velocity on both its performance and its effects on the surrounding ground. The computational effort required to simulate the dynamic TES operation is investigated comparing a model using a fully coupled GW flow-heat transfer approach, in which temperature and velocity field are solved at each iteration, and a model using a decoupled approach, where the GW flow field is directly applied to the heat transfer equation.

2. Methods

Defining an effective modelling set-up to investigate the interaction between GW and underground TES is fundamental to support a design that complies to specific environmental requirements for GW protection and to ensure an optimal performance of the TES. A simplified sketch of the investigated underground TES is presented in Fig. 1.

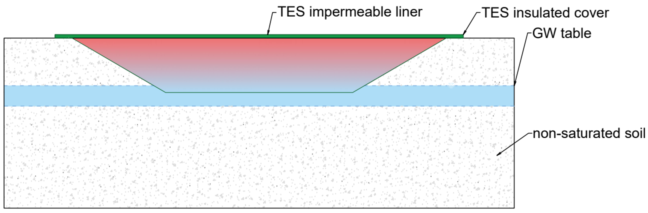

Fig. 1: Characteristic design of underground pit TES storage in presence of an aquifer.

2.1 Governing equations

The energy balance of the TES water domain is modelled using a system of partial differential equations (see eq. 1, for one segment i), where the thermal losses term $\dot{q}_{loss,i}$ couples the TES water domain and the soil domain. Eq. 2 presents the general formulation for the energy balance of the ground; the convective term is included only in the layer hosting the GW table.

$$\rho A_i c_p \frac{\partial T_i}{dt} = \rho \dot{V} c_p \nabla T_i + A_i \nabla \cdot (\lambda_{eff,mix} \nabla T) - \dot{q}_{loss,i} \tag{1}$$

$$\rho_p c_{p,p} \frac{\partial T_p}{\partial t} = (\nabla \cdot \lambda_p \nabla T_p) - \rho_f c_{p,f} u_s \cdot \nabla T_p + \dot{q}_{loss,i} \tag{2}$$

2.2 Elements of groundwater modelling

The flow of water through porous media like soil is governed by Darcy's law (eq. 3). The Darcy flow u_s is driven by the difference of hydraulic head H_{gw}, the driving force for liquid flow, and the hydraulic conductivity K_F, which is a measure of ease with which a fluid flows through the porous matrix.

$$u_s = -K_F \cdot \nabla H_{gw} \tag{3}$$

The hydraulic conductivity is a function of the permeability κ of the porous medium (by eq. 4) and the fluid properties (density ρ and dynamic viscosity μ). Hence, in numerical modelling the most common definition of the Darcy's law is the one provided by eq. 5, which correlates the Darcy flow u_s to the material permeability and the pressure drop in the porous medium.

$$K_F = \frac{\kappa \rho g}{\mu} \tag{4}$$

$$u_s = -\kappa / \mu \nabla p \tag{5}$$

Soil permeability depends on the pore size, the pore connectivity, the grain size and the packing of the grains. The Kozeny-Carman equation provides a classical formulation for estimating permeability based on these parameters. In hydrogeology, soil properties are commonly described in terms of hydraulic conductivity. Typical ranges of hydraulic conductivity for different soil materials are reported in Tab. 1.

Tab. 1: Representative ranges of effective porosity and hydraulic conductivity for unconsolidated soil materials, from (Freeze et al. 1979) and (Woessner et al. 2024), and thermal conductivity ranges for moist/saturated conditions (VDI 2010 as reported from (Dalla Santa et al. 2020)). The effective porosity defines the fraction of interconnected pore space through which GW can actually flow.

Soil	**Effective porosity**	K_F **/ [m/s]**	λ **/ [W/(m·K)]**
Clay/Silt	0.10–0.30	10^{-9} – 10^{-6}	1.0-3.0
Sand	0.15–0.40	10^{-6} – 10^{-3}	1.0-3.0
Gravel	0.15–0.45	10^{-3} – 10^{-1}	1.6-2.5

2.3 Numerical model implementation

The numerical model is implemented in COMSOL Multiphysics environment using the modules 'Heat Transfer in Solids' to investigate the heat transfer in the ground and in the aquifer according to eq. 2 and 'Coefficient Form PDE' to model the energy balance of the TES water domain by eq. 1 (Tosatto et al. 2024). The Darcy flow field of the GW is modelled using the 'Coefficient Form PDE', implementing eq. 5.

A reference TES case without GW flow is presented using the COMSOL model cross-validated within the work of the IEA ES Task 39 (Schmidt et al. 2024). The absence of GW flow and the axial symmetry of the geometry allows to simplify the simulation to a 2D axisymmetric study.

In the presence of a directional GW flow, a 3D model of the ground is necessary as the axial symmetry of the problem is not any more applicable. This increases the complexity in the evaluation of the coupling effects (i.e., the thermal losses) between the TES and the ground and requires significantly larger computational effort. However, the system retains reflection symmetry with respect to a vertical plane aligned with the mean GW flow direction, hence half of the domain is considered to reduce the computational effort. In the 3D model, the circumferentially averaged temperature of the ground in contact with the TES ($T_{g,bc}(z,t)$) is obtained by projecting the 3D temperature field from the lateral surface onto the longitudinal axis representing the TES fluid domain using the 'General Projection' operator available in COMSOL Multiphysics. The mantle surface is parametrized in terms of the axial coordinate z and the circumferential angle θ, which map each point on the boundary to a unique position in the (z, θ) parameter space.

In a coupled approach, the GW flow field is solved at each simulation step together with the ground heat transfer equation. A second approach is tested, in which the GW velocity field is solved in a preliminary step using the sole Darcy equation for the GW domain in steady state conditions, assuming the fluid viscosity and density and the effective soil thermal conductivity as independent from the temperature. This allows to directly use the derived velocity field in the dynamic model that solves the energy balance equations for the TES, the soil and the GW layer, without the need to solve the Darcy equation for all the mesh elements at every single time step.

2.4 Case Study

The underground tank TES (TTES-1-UG) and shallow pit TES (PTES-1-C) geometries from IEA ES Task 39 are investigated. The geometric details are presented in Table 2. In order to understand the influence of GW characteristics, the investigation of the PTES-1-C is extended to consider the case with shallow GW (at 5 m depth from ground surface, *'shallow GW'*) and with GW below the TES (1 m below the TES, 17 m from ground surface, *'below TES GW'*). The three GW configurations are presented in Figure 2.

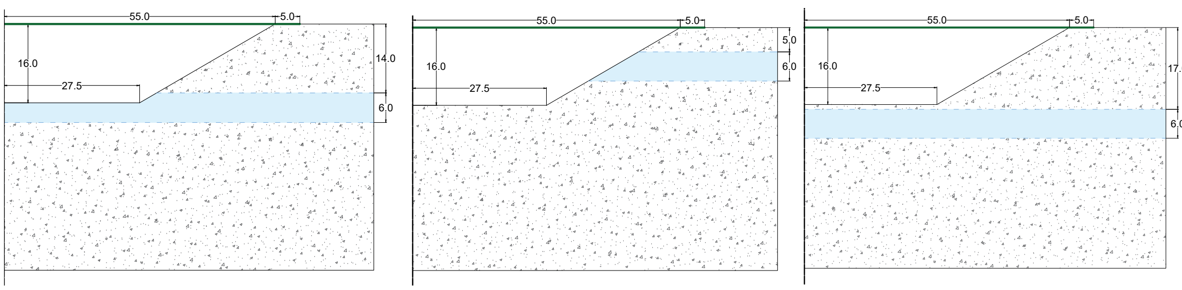

(a) PTES with deep GW. **(b)** PTES with shallow GW. **(c)** PTES with GW below TES.

Fig. 2: Investigated PTES with different location of GW.

Both insulated and uninsulated TES configurations are considered. A cover extension of 5 m is applied in all TES configurations. The soil properties used to model the GW layer in the numerical model are presented in Table 3. In this analysis no geotechnical GW protection measures (beyond insulation) are considered. The influence of the Darcy flow velocity is investigated with two additional cases: u_s=2.5×10^{-6} m/s and u_s=1.5×10^{-5} m/s, while the ground permeability is kept constant.

A purely seasonal TES operation is considered in this study, with one yearly phase of charge and discharge separated by a brief storage period, as summarised in Table 4. The storage operates between 90 and 30 °C, the ambient air presents a seasonal oscillation between 0 and 20 °C, while the undisturbed ground temperature is

Tab. 2: Investigated TES configurations for TTES-1-UG and PTES-1-C test cases, including geometry and envelope characteristics.

Parameter	TTES-1-UG	PTES-1-C
Location	Underground	Underground
TES exact volume	100,961 m^3 water volume	99,404 m^3 water volume
Geometry		
Shape	Cylinder	Cone (truncated, inverted)
Height / Diameter	H = 27 m; D = 69 m	H = 16 m; D_{top} = 119 m; d_{bottom} = 55 m
Additional parameters	–	Wall slope 1:2 (26.6°)
Insulation		
Top insulation	U_{top} = 0.1 W/(m^2·K), horizontal extension: 5 m	
Side/bottom	w/o insulation: h_{side} = h_{bottom} = 90 W/(m^2·K)	
	w insulation: h_{side} = h_{bottom} = 0.15 W/(m^2·K)	

Tab. 3: Soil properties and GW conditions adopted for the investigated cases, from IEA ES Task 45 (IEA Energy Storage TCP 2026).

Property	Symbol	Unit	Value
Thermal properties			
Specific heat capacity	$c_{p,s}$	J/(kg·K)	1333.3
Thermal conductivity	λ	W/(m·K)	2.4
Thermal diffusivity	α	J/(m·d·K)	207360
Hydraulic properties			
Density	ρ_s	kg/m^3	2100
Volume fraction	θ_s	%	65
Porosity	φ_A	%	35
Hydraulic conductivity	K_F	m/s	1.15×10^{-4}
Groundwater flow conditions			
Difference of hydraulic head	∇H_{gw}	m	14.5
Hydraulic gradient	i	–	0.06938
Superficial velocity (Darcy flow)	u_s	m/s	7.98×10^{-6}
Longitudinal thermal dispersivity	α_L	m	5
Transverse thermal dispersivity	α_T	m	0.5

assumed to be 10 °C. An operation period of 10 years is simulated, to account for the pre-heating of the ground. The first 8 years of operation are simulated with a larger time-stepping to reduce the computational effort, while the last two years are simulated with a solver-controlled step size of maximum 10,800 s (3 h).

Tab. 4: TES operation (inlet/outlet volumetric flow, inlet temperatures) for one year, from IEA ES Task 45 (IEA Energy Storage TCP 2026).

Time interval [h]	Phase	V [m^3/h]	T_{in} [°C]
0–2919	Charge	−30	90
2920–3649	Storage	0	–
3650–6569	Discharge	30	30
6570–8760	Idle	0	–

The performance indicators used to assess the influence of GW on TES are the TES internal energy, thermal losses and water vertical temperature stratification on the 10th year of TES operation. To evaluate the twofold effect on the ground, the ground temperature is assessed in the region downstream of the TES, which is the zone most affected by overheating. The locations of the temperature probes in the ground are presented in Fig. 3, while Tab. 5 provides the location and labels of the single probes.

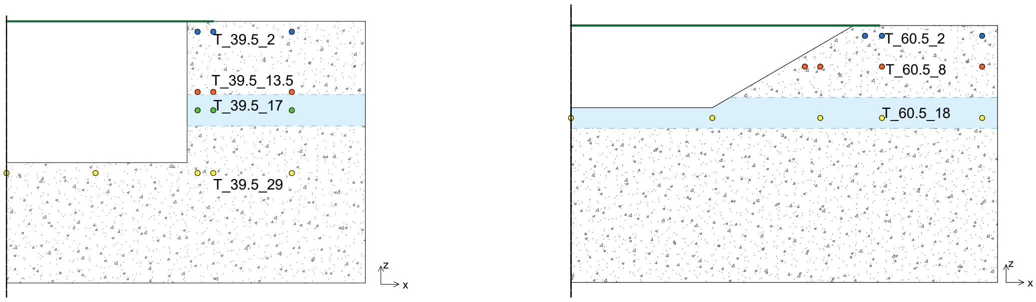

Fig. 3: Location of the ground probes in the TTES (left figure) and PTES (right figure).

Tab. 5: Ground temperature sensor coordinates and data point labels for case TTES-1-UG and PTES-1-C. The sensor layout is shown in Fig. 3. Daily mean values are reported.

TTES-1-UG					
Vertical distance from ground surface [m]	Horizontal distance from centre [m]				
	0	17	36.5	39.5	54.5
2	–	–	T_36.5_2	T_39.5_2	T_54.5_2
13.5	–	–	T_36.5_13.5	T_39.5_13.5	T_54.5_13.5
17	–	–	T_36.5_17	T_39.5_17	T_54.5_17
29	T_0_29	T_17_29	T_36.5_29	T_39.5_29	T_54.5_29

PTES-1-C							
Vertical distance from ground surface [m]	Horizontal distance from centre [m]						
	0	27.5	45.5	48.5	57.5	60.5	80
2	–	–	–	–	T_57.5_2	T_60.5_2	T_80_2
8	–	–	T_45.5_8	T_48.5_8	–	T_60.5_8	T_80_8
18	T_0_18	T_27.5_18	–	T_48.5_18	–	T_60.5_18	T_80_18

3. Results

The GW flow field is solved for the aquifer layer. The presence of the underground storage creates a disturbance of the flow, which needs to deviate, increasing its velocity on the side of the TES. Fig. 4 presents the GW flow field resulting from a stationary study solving eq.5.

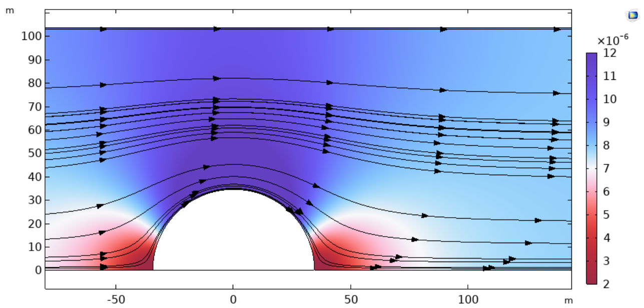

Fig. 4: Darcy velocity magnitude (surface plot, m/s) and flow field (streamlines) solved for the TTES geometry (top view, xy plane).

GW flowing through the surrounding ground, past the outer TES walls, results in an asymmetric heat flux (and temperature) distribution in the ground in the xy plane, with a thermal plume forming downstream of the TES. At each height z_i, the ground temperature over the mantle surface in contact with the TES lateral walls is spatially averaged and used as boundary condition for the $\dot{q}_{loss,i}$ term in eq. 1. Fig. 5 illustrates this for the insulated TTES on the last day of storage operation: the 3D temperature distribution (left figure) is averaged into the 1D profile shown in red (right), alongside local vertical temperature profiles at three angular positions — upstream at 180°, mid at 90° and downstream at 0° — shown for reference.

As a first comparison, the TES internal energy relative to the average ambient temperature (10°C) is used to compare the reference 2D TES (no GW flow) with the case including GW flow. The results for the two TES geometries are presented in Fig. 6.

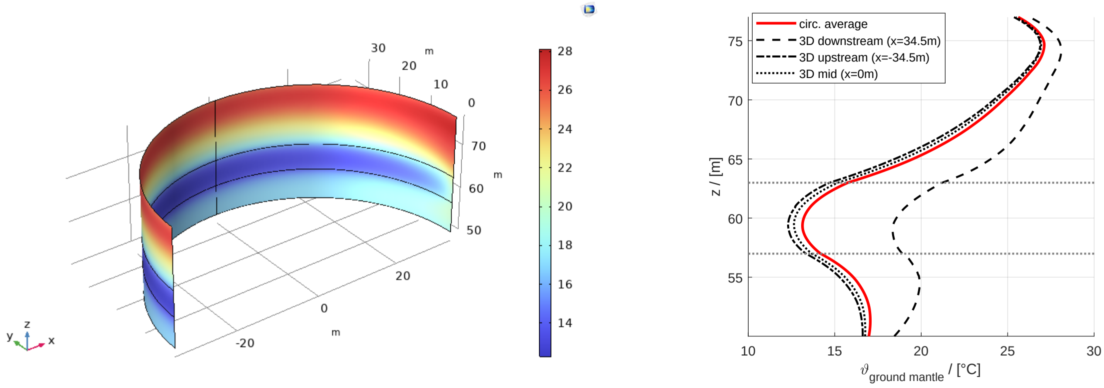

Fig. 5: 3D temperature distribution of the ground in contact with the TES (left) and comparison between local vertical temperature profiles and the circumferentially averaged mantle temperature (right) for the insulated TTES with GW flow (last simulation step). The zone of the aquifer is delimited by the horizontal lines.

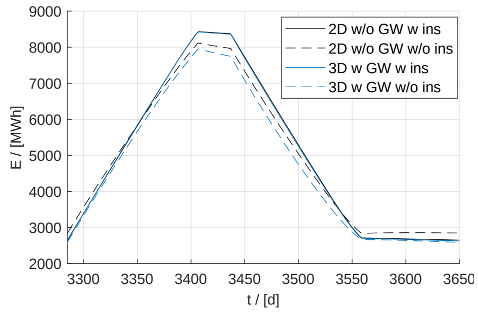

(a) TTES

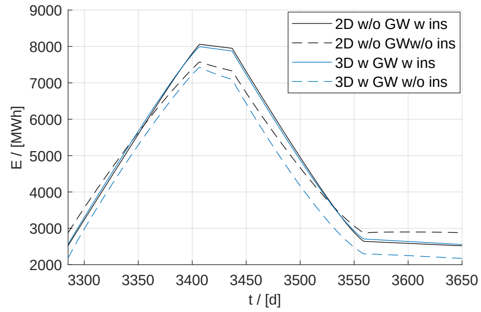

(b) PTES

Fig. 6: Internal energy profile during the 10th year of TES operation for the investigated cases (GW depth 14 m, u_s=7.98E-6 m/s).

Internal energy is an aggregated KPI, however, and cannot capture the local impact of GW flow on the ground or on the TES performance. Fig. 7 therefore breaks down the TES thermal losses for the 10th year of operation by envelope element. The effect of GW flow is most visible in the uninsulated case, where the lack of insulation increases the local advective losses from the sidewalls and (for the PTES) from the bottom wall. For the same GW depth and flow rate, the uninsulated PTES shows markedly higher thermal losses than the TTES, most likely due to its larger envelope surface invested by the GW flow (2.5 times that of the TTES, considering both side and bottom surface).

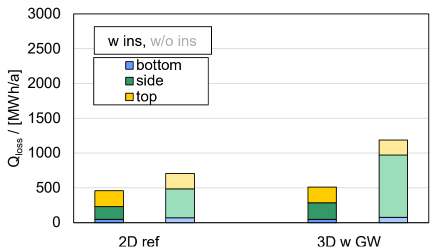

(a) TTES

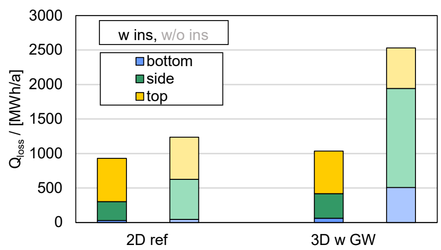

(b) PTES

Fig. 7: Breakdown of the thermal losses during the 10th year of operation (GW depth 14 m, u_s=7.98E-6 m/s).

The increased advective heat transfer results in a loss of thermal stratification in the water domain, reducing the TES exergy content. The temperature profiles during the last year of operation for the cases presented in Fig. 7 are shown in Fig. 8; thermal stratification provides a direct measure of the quality of energy available for discharge. Fig. 9 provides a detail of the vertical thermal stratification for the four cases for the time steps corresponding to the end of the charging phase, end of the storage phase and mid discharge phase. With side and bottom wall insulation, GW flow has little effect on the TES outlet temperature. Without insulation (dashed lines), however, the increased losses affect both geometries. In the TTES (Fig. 8b), where GW flow crosses the mid-height section, the lack of insulation causes a temperature drop of about 5–10 K during discharge, relative to the insulated case. In the PTES (Fig. 8d), this effect is less pronounced, as GW flow crosses the lower part of the tank; the resulting drop in outlet temperature during discharge nonetheless ranges between 5 and 10 K.

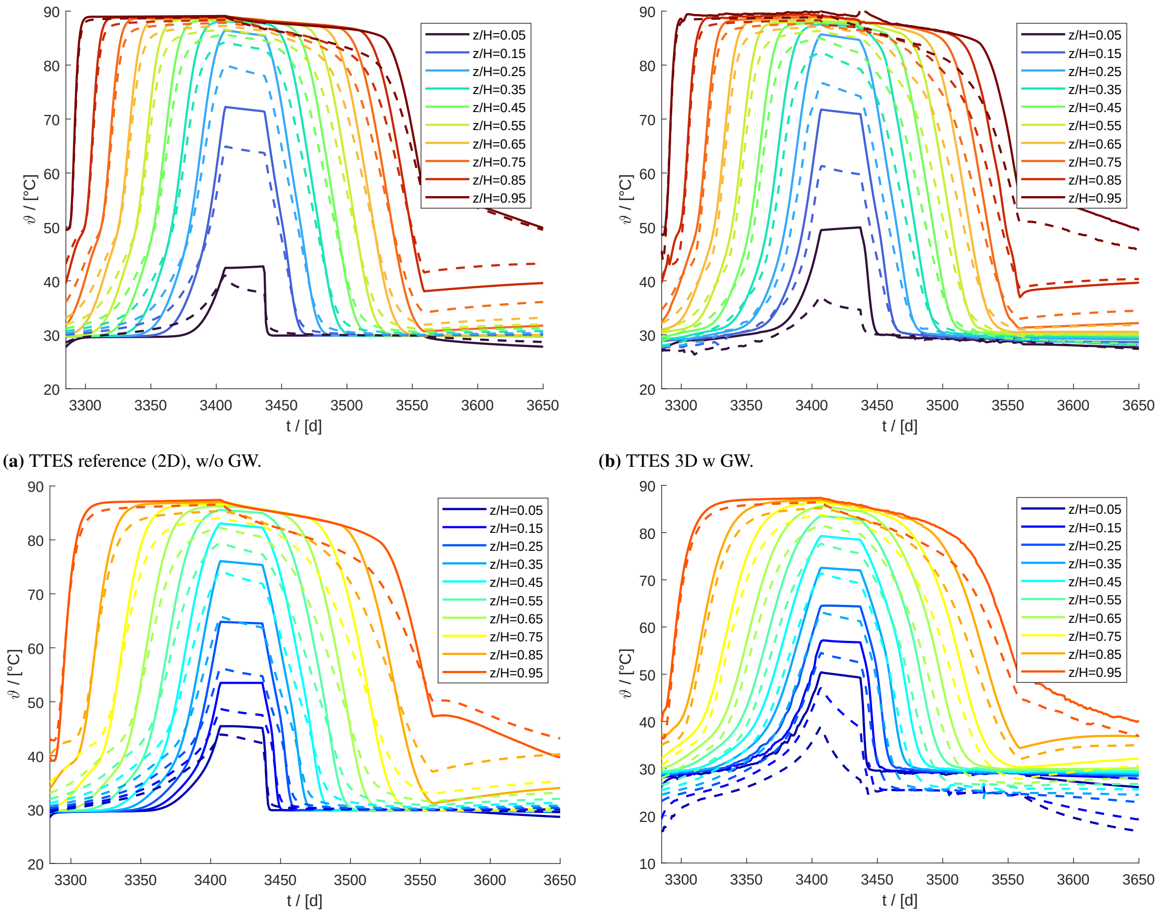

(a) TTES reference (2D), w/o GW.

(b) TTES 3D w GW.

(c) PTES reference (2D), w/o GW.

(d) PTES 3D w GW.

Fig. 8: Temperature profile during the 10th year of operation (GW depth 14 m, u_s=7.98E-6 m/s). The dashed lines present the uninsulated case, the continuous line the insulated one.

Assessing the full impact of GW flow also requires considering its effect on the ground and on the GW itself. Fig. 10 shows the ground temperature distribution for the uninsulated TES cases, evaluated early in the discharging phase (day 3500) to account for the thermal inertia of the ground. As this represents the worst case in terms of thermal losses, it highlights where GW flow has the greatest influence: a thermal plume driven by advective transport is clearly visible within the aquifer layer downstream of the TES.

Fig. 11 shows the ground temperature profiles recorded within the GW layer during the 10th year of operation, for both insulated and uninsulated cases. The effect of insulation in limiting the overheating of the GW is clearly visible. A further relevant aspect is the time delay in the ground temperature rise, observed at three monitoring points located at increasing distance from the TES. The TTES represents the worst case for GW overheating, since the aquifer crosses the central part of the tank: this results in a downstream peak temperature of up to 70°C at 5 m from the TES wall, and up to 60°C at 20°m, occurring at the end of the discharge period. In the PTES case, GW overheating is limited, as the aquifer is in contact only with the bottom of the tank, which under the given operating conditions remains close to 30°C (the DH return temperature) for most of the year. The presence of GW in the lower part of the TES (PTES case) does not result in significant ground temperature increases, but it is worthy reminding that this storage operates between 90 and 30°C, so higher return temperature from the DH network, in absence of thermal insulation will directly result in higher GW temperatures in this case.

Table 6 summarizes the computational cost of simulating one year of TES operation. All simulations employed a time-dependent solver with free, solver-controlled time stepping, subject to a maximum time-step constraint of 10,800 s (3 h). Simulations were run on a PC equipped with an Intel(R) Core(TM) i5-8350U CPU (4 cores,

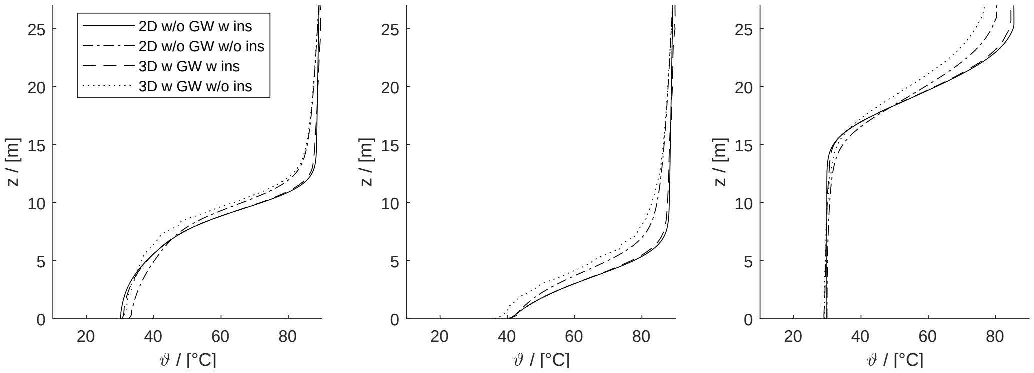

(a) TTES

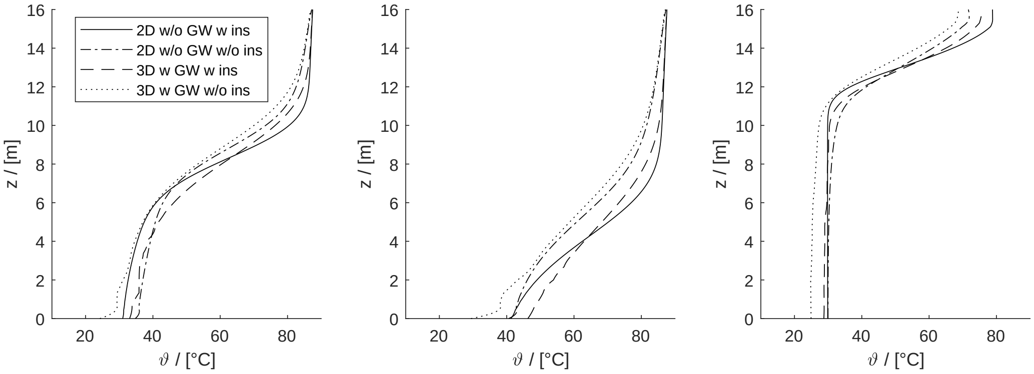

(b) PTES

Fig. 9: TES temperature profile for the TTES (top) and PTES (bottom) at day 3405 (left), 3435 (center) and 3555 (right) of the 10 year operation period (GW depth 14 m, u_s=7.98E-6 m/s).

8 threads) and 16 GB RAM. In the models including the GW flow, the ground mesh was refined in the aquifer layer and in the nearby ground, thus increasing the number of domain elements. The results of the comparison show that including GW in the analysis significantly increases the simulation time, but the application of a decoupled approach allows to save ≈20% of simulation time, with no loss of accuracy.

Tab. 6: Computational details of the numerical models implemented for the PTES and simulation time for a period of 1 year of operation.

Parameter	2D-thermal	3D-thermal	3D-w GW	3D-w GW (decoupled)
Model configuration				
Spatial dimension	2D	3D, half domain	3D, half domain	3D, half domain
Solution approach	w/o GW	w/o GW	coupled GW flow-thermal	decoupled GW flow-thermal
Simulated period	1 year	1 year	1 year	GW flow: steady state thermal: 1 year
Mesh				
Element type	Free tetrahedral	Free tetrahedral	Free tetrahedral	Free tetrahedral
No. of domain elements	1615	32,962	124,515	124,515
Element size range	0.56–10.8 m	0.69–34.2	0.7–35.3 m	0.7–35.3 m
Min. element quality*	0.3432	0.3201	0.3013	0.3013
Avg. element quality*	0.8875	0.5743	0.6853	0.6853
Simulation time				
Solve time	≈ 3 min 17 s	≈ 28 min 28 s	≈ 8 h 38 min	GW flow: ≈ 5 s thermal: ≈ 6 h 44 min

* numerical value between 0.0 (degenerated element) and 1 (best possible element) measuring the regularity of mesh elements' shapes

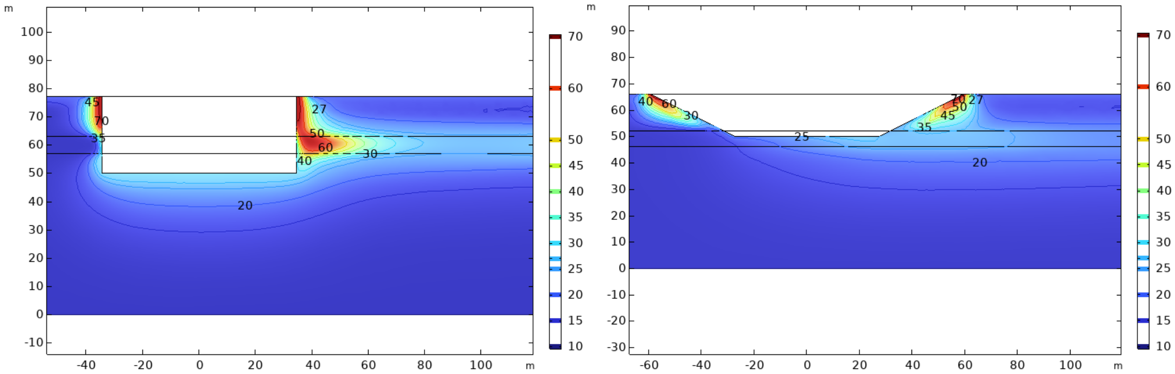

(a) TTES w GW, w/o ins.

(b) PTES w GW, w/o ins.

Fig. 10: Ground temperature distribution in the TES cases without insulation (t: 3500 d, GW depth 14 m, u_s=7.98E-6 m/s).

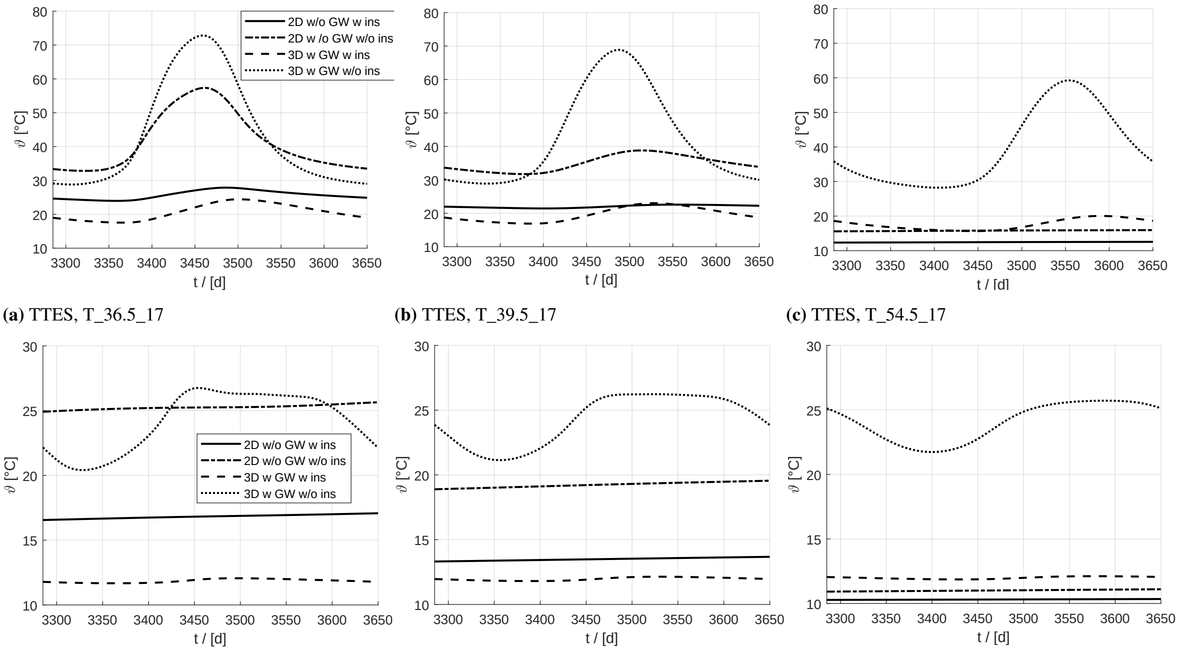

(a) TTES, T_36.5_17

(b) TTES, T_39.5_17

(c) TTES, T_54.5_17

(d) PTES, T_48.5_18

(e) PTES, T_60.5_18

(f) PTES, T_80_18

Fig. 11: Ground temperature in the sensors located in the GW layer (GW depth 14 m, u_s=7.98E-6 m/s), for the TTES ((a) to (c)) and PTES ((d) to (f)).

3.1 Influence of GW depth

The PTES geometry is the most common solution for seasonal storage, and most existing projects do not present lateral and bottom insulation. In the presence of GW flow this could be a problem, depending on local regulations and GW characteristics. Three different GW depths are hence investigated to provide a sensitivity analysis of the twofold impact between TES and GW. The breakdown of thermal losses is presented in Fig. 12.

The location of the GW relative to the TES thermal stratification has a significant impact on TES performance: when the aquifer is in contact with the high-temperature upper section of the TES, losses are higher. However, even without direct contact between the TES and GW (i.e. GW below the TES at a depth of 17 m), increased thermal losses still occur through the side and bottom walls in the absence of insulation.

The effect on the surrounding ground is presented in Fig. 12, which shows the temperature profile at the ground sensor located 8 m below the ground surface, 48.5 m from the TES symmetry axis. For the case with GW depth of 5 m, this sensor lies directly within the aquifer layer, resulting in lower recorded temperatures due to the enhanced heat removal by GW advection.

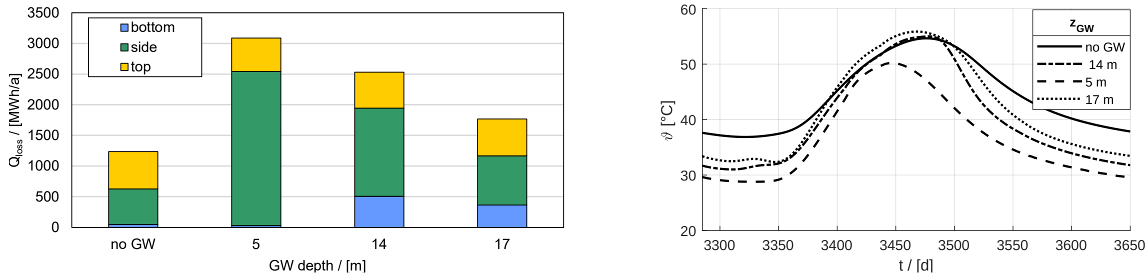

Fig. 12: Breakdown of the thermal losses (left figure) and ground temperature at sensor position T_48.5_8 (right figure) during the 10th year of operation for the uninsulated PTES at different GW depths (u_s=7.98E-6 m/s).

3.2 Influence of GW flow velocity

In the PTES case with deep GW (depth 14 m), the aquifer flows past the lower zone of the PTES. From the results on the previous paragraphs, for the given GW flow velocity, the overheating effect even in absence of thermal insulation is lower than the case of shallow GW. Fig. 13 presents the influence of the GW flow velocity on the thermal losses and ground temperature (sensor T_48.5_18). The range of velocities considers the typical values for sand/gravel aquifers. The results are consistent with the observations of previous studies, with an increase of thermal losses with increasing GW flow. The ground temperatures on the observation point in presence of GW are affected by the seasonality of the PTES cycles and show lower temperatures with increasing GW flow velocity. An important remark is, however, necessary: eq. 3 shows that GW flow velocity depends on both the local soil characteristics, which can be assumed constant, and the hydraulic gradient, which varies seasonally depending on the location due to changes in water table recharge (higher in spring), snowmelt timing and precipitation cycles.

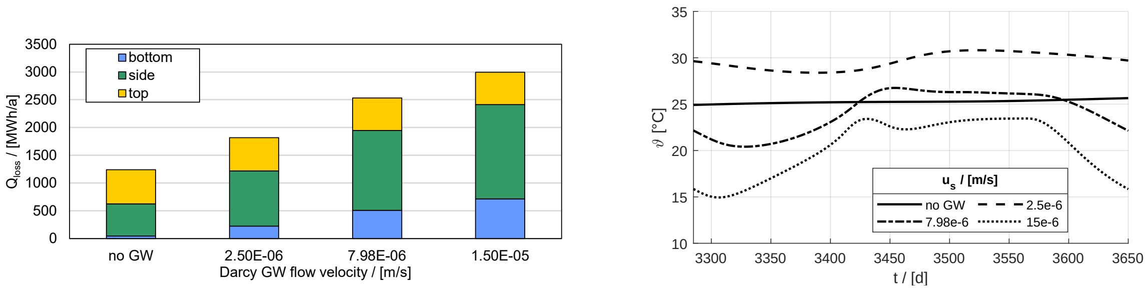

Fig. 13: Breakdown of the thermal losses (left figure) and ground temperature at sensor position T_48.5_18 (right figure) during the 10th year of operation for the uninsulated PTES for different Darcy GW flow velocities (GW depth 14 m).

4. Conclusions

This study investigated the numerical modelling of underground TES operating in the presence of GW flow, focusing on how advective transport reshapes the thermal interaction between the storage and its surrounding ground. The results show that GW flow does not simply add a uniform loss term to the TES energy balance: its impact is strongly geometry- and insulation-dependent, and it manifests differently depending on which part of the TES envelope is in contact with the aquifer. This highlights the limitation of aggregated performance indicators, such as internal energy, which mask these localized effects and can therefore lead to an incomplete assessment of TES performance in GW-affected sites.

More broadly, the comparison between insulated and uninsulated TES configurations confirms that envelope insulation remains an important lever for limiting GW-driven losses, but its relative importance depends on the storage geometry. Similarly, the results show that GW flow effects on TES performance cannot be evaluated independently of the surrounding ground: the persistence of a downstream thermal plume, and the delayed but sustained temperature rise observed away from the TES walls, indicate that GW flow acts as a long-term thermal transport mechanism whose effects extend well beyond the storage boundary itself. This has direct implications for the design and siting of underground TES systems, since the assessment of thermal losses alone is not sufficient to characterize the environmental impact of the storage on the aquifer.

The comparison of the simulation effort required shows that resolving GW flow raises the computational cost of TES simulations by more than two orders of magnitude relative to thermal-only models, but the proposed decoupled formulation recovers a substantial share of this cost with no loss of accuracy.

Future work should extend this analysis to the investigation of numerical models with detailed representation of the TES envelope, in particular for TTES geometries, to consider the thermophysical effects of massive side walls and GW protection measures.

5. Acknowledgement

References

Blum, Philipp et al. (2021). "Is thermal use of groundwater a pollution?" In: *Journal of Contaminant Hydrology* 239, p. 103791. DOI: 10.1016/j.jconhyd.2021.103791.

Bott, Christoph et al. (2024). "Influence of thermal energy storage basins on the subsurface and shallow groundwater". In: *Journal of Energy Storage* 92, p. 112222. DOI: 10.1016/J.EST.2024.112222.

Dahash, Abdulrahman et al. (2021). "Understanding the interaction between groundwater and large-scale underground hot-water tanks and pits". In: *Sustainable Cities and Society* 71, p. 102928. DOI: 10.1016/j.scs.2021.102928.

Dalla Santa, Giorgia et al. (2020). "An updated ground thermal properties database for GSHP applications". In: *Geothermics* 85, p. 101758. DOI: https://doi.org/10.1016/j.geothermics.2019.101758.

Freeze, R. Allan and John A. Cherry (1979). *Groundwater*. Englewood Cliffs, New Jersey: Prentice-Hall.

Haehnlein, Stefanie, Peter Bayer, and Philipp Blum (2010). "International legal status of the use of shallow geothermal energy". In: *Renewable and Sustainable Energy Reviews* 14.9, pp. 2611–2625. DOI: https://doi.org/10.1016/j.rser.2010.07.069.

IEA Energy Storage TCP (2024). *IEA ES TCP Task 39 - Large Thermal Energy Storages for District Heating. Deliverable A5 - List of LTES projects*. URL: https://iea-es.org/task-39/deliverables/.

— (2026). *Task 45: Accelerating the Uptake of Large Thermal Energy Storages*. Accessed on 4 September 2026. URL: https://iea-es.org/task-45/.

Lüchinger, Richard et al. (2025). "Cost Analysis for Large Thermal Energy Storage Systems". In: *ASME Journal of Engineering for Sustainable Buildings and Cities* 6 (2). DOI: 10.1115/1.4069122.

Motamedi, Mohammadhossein et al. (2026). "When heat meets water: Environmental trade-offs of underground thermal energy storage". In: *Journal of Energy Storage* 149, p. 120265. DOI: 10.1016/J.EST.2025.120265.

ÖWAV (2009). *ÖWAV-Regelblatt 207: Thermische Nutzung des Grundwassers und des Untergrunds – Heizen und Kühlen*. Wien, Austria: Österreichischer Wasser- und Abfallwirtschaftsverband (ÖWAV).

Schmidt, T. et al. (2024). *IEA ES TCP Task 39 - Large Thermal Energy Storages for District Heating. Subtask C: Round Robin Simulations*. Tech. rep. URL: https://iea-es.org/task-39/deliverables/.

Schmidt, Thomas et al. (2018). "Design Aspects for Large-scale Pit and Aquifer Thermal Energy Storage for District Heating and Cooling". In: *Energy Procedia*. Vol. 149. Elsevier Ltd, pp. 585–594. DOI: 10.1016/j.egypro.2018.08.223.

Sifnaios, Ioannis et al. (2023). "Heat losses in water pit thermal energy storage systems in the presence of groundwater". In: *Applied Thermal Engineering* 235, p. 121382. DOI: 10.1016/J.APPLTHERMALENG.2023.121382.

Tosatto, Alice and Fabian Ochs (2024). "Comparison of detailed large-scale Thermal Energy Storage simulation models". In: *Proceedings of BauSim Conference 2024: 10th Conference of IBPSA-Germany and Austria*. IBPSA-Germany and Austria, pp. 18–25. DOI: 10.26868/29761662.2024.3.

VDI (2010). *VDI 4640 Blatt 1: Thermal use of the underground – Fundamentals, approvals, environmental aspects*. Verein Deutscher Ingenieure e.V. URL: https://www.vdi.de/en/home/vdi-standards/details/vdi-4640-blatt-1-thermal-use-of-the-underground-fundamentals-approvals-environmental-aspects (visited on 08/07/2026).

Woessner, William W. and Eileen P. Poeter (2024). *Hydrogeologic Properties of Earth Materials and Principles of Groundwater Flow*. Accessed on 4 September 2026. Guelph, Ontario, Canada: The Groundwater Project. URL: https://books.gw-project.org/hydrogeologic-properties-of-earth-materials-and-principles-of-groundwater-flow/.